ACS APPLIED ENERGY MATERIALS

www.acsaem.org Article

Dual Function of Surface Alkali-Gas Erosion on SnO_2 for Efficient and Stable Perovskite Solar Cells

Hao Huang,[‡] Xin Liu,[‡] Mingjun Duan, Jun Ji, Haoran Jiang, Benyu Liu, Sajid Sajid, Peng Cui, Dong Wei, Yingfeng Li, and Meicheng Li*

Cite This: *ACS Appl. Energy Mater.* 2020, 3, 5039−5049 Read Online

ACCESS | Metrics & More | Article Recommendations | Supporting Information

ABSTRACT: The electrical character and interface contact of the electron transport layer (ETL) play a critical role in high-efficiency planar perovskite solar cells. Here, a dual functional surface alkali-gas erosion (SAE) method is proposed based on the unique chemical properties of the amphoteric oxide. First, during the SAE process, SnO_2 can react with alkaline gas slightly, and the chemical reaction mechanism is elucidated, which leads to the crystal fusion of the SnO_2 surface, bringing an improved electron mobility and an excellent interface contact between the SnO_2 ETL and perovskite layer. Second, the SAE method introduced the $-NH_2$ group on the SnO_2 surface chemically, which can provide a nucleation site for the perovskite crystal and promote the growth of the perovskite film; meanwhile, the $-NH_2$ group connected chemically with SnO_2 also serves as a bridge-link by replacing the organic cation at the perovskite/SnO_2 interface, which effectively enhances the interfacial charge transport and the perovskite crystallinity. As a consequence, devices with SAE achieve a champion PCE of 21.10%, and the average PCE is increased from 18.07 to 20.30%, which mainly results from the increase of short-circuit current density from 22.34 to 24.19 mA cm^{-2}. Moreover, the optimized devices retain 86% of its initial PCE (compared with 41% of the control device) after 60 days at room temperature with 40−50% humidity.

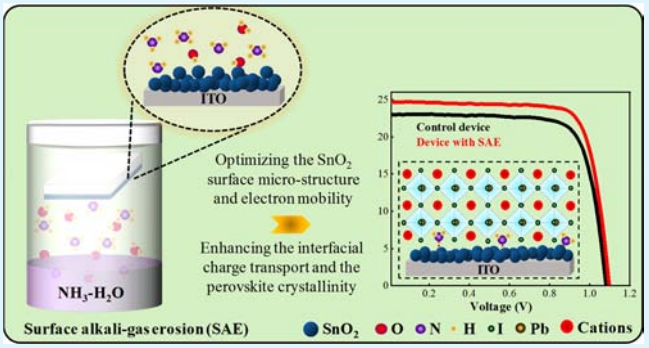

KEYWORDS: *Perovskite solar cells, Surface alkali-gas erosion, Surface morphology modulation, Interfacial bonding, Crystal nucleation*

HIGHLIGHTS

(1) A simple method using the available materials in daily life is introduced for the first time to simultaneously reshape the SnO_2 surface morphology and enhance SnO_2/perovskite interfacial charge transfer to further improve the device performance.

(2) The chemical reaction mechanism between SnO_2 and alkaline gas during the SAE method is elucidated based on the unique chemical properties of the amphoteric oxide, which demonstrates that the SAE method could also be used to other amphoteric oxide ETLs.

(3) The perovskite crystal nucleation process and mechanism are elucidated after the $-NH_2$ group has been introduced at the SnO_2/perovskite interface.

INTRODUCTION

Organic−inorganic metal halide perovskite solar cells (PSCs) have attracted huge attention due to their excellent performance and low-cost solution-processable fabrication since they have been reported for the first time in 2009 with a power conversion efficiency (PCE) of 3.8%.[1] Recently, various technologies have been proposed to obtain high-efficiency PSCs, including perovskite-film optimization, defect passivation, interface engineering, and device structure engineering.[2−6] To date, owing to its simple structure, easy preparation, and flexible application, the most popular cell structure is planar-type with a compact electron transport layer (ETL). For planar PSCs, the metal oxides such as TiO_2, SnO_2, and ZnO applied as ETLs have been widely researched due to their excellent photoelectric properties and commercial availability.[7−10] Among them, SnO_2, as a type of inorganic metal oxide, has a band gap about 3.6 eV and a suitable conduction band, which has a good alignment with the conduction band of perovskite. Furthermore, SnO_2 ETL exhibits excellent chemical stability, and it is insensitive to UV light, which can help to obtain PSCs with long-term stability.[8,11,12]

Applying SnO_2 as ETL has attracted lots of attention since it has been reported by Fang's group in 2015.[13] Over the last few

Received: March 19, 2020
Accepted: April 24, 2020
Published: April 24, 2020

https://dx.doi.org/10.1021/acsaem.0c00563
ACS Appl. Energy Mater. 2020, 3, 5039−5049

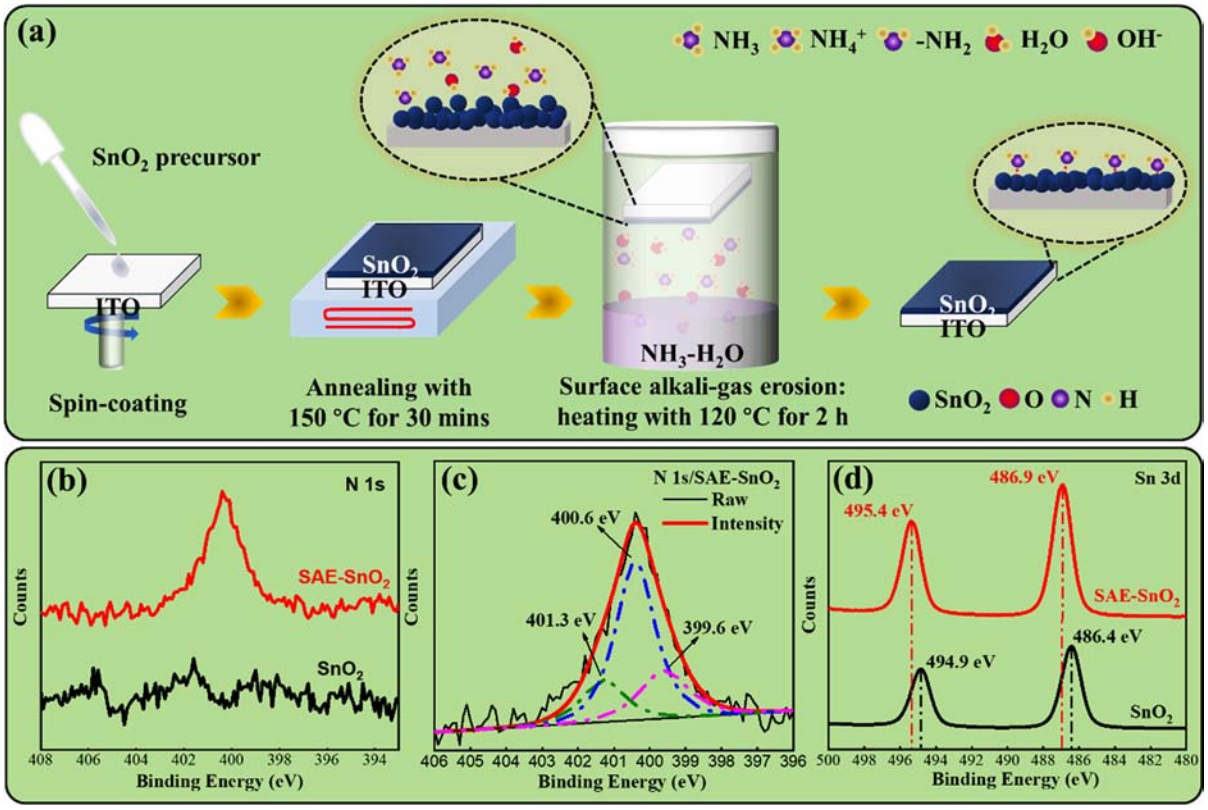

Figure 1. Schematic of surface alkali-gas erosion procedures and characterization of ETLs. (a) Schematic of surface alkali-gas erosion procedures. (b) The N 1s XPS spectra of ETLs. (c) The analysis of N 1s XPS spectra of ETLs. (d) The Sn 3d XPS spectra of ETLs.

years, in order to obtain high-quality SnO_2 films, various preparation methods have been proposed, such as solution spin-coating,[14,15] atomic layer deposition,[16] chemical bath deposition,[16,17] and magnetron sputtering deposition.[18] Among these methods, it is worthy to note that the solution spin-coating using commercial SnO_2 aqueous colloidal dispersion solution is especially available and convenient.[8] To improve device efficiency, it is reported that doping La,[19] Li,[20] Mo,[21] Y,[22] Zn,[23] and other elements in SnO_2 films could effectively improve electronic conductivity and tune the Fermi-level position for obtaining good alignment with the perovskite film.[24−27] The additives ethylene diamine tetraacetic acid (EDTA)[28] and Red-Carbon-Quantum-Dot[29] in commercial SnO_2 aqueous colloidal dispersion solution have been applied to optimize microstructure-morphology and decrease the surface energy of the SnO_2 film, which could passivate surface defects and increase perovskite crystallization. To reshape the surface morphology is also an available way to optimize performance of ETL, for example, combining the additives EDTA[28] and NH_4Cl[30] in the SnO_2 precursor solution could slightly decrease the surface roughness of the SnO_2 film, and fabrication of the SnO_2/TiO_2 nanowire-nanoshell structure could effectively enhance electron injection and collection.[31] These studies show the importance of ETL to the efficiency of planar PSCs and a vital significance for further studies of the SnO_2 film as ETL.

Besides the ETL itself, the heterojunction interface composed of ETL and perovskite also plays a vital role in planar PSC performance. Due to the different chemical properties of inorganic metal oxide and organic−inorganic perovskite, there exists a mass of defects at the interface that can result in loss of photon-generated carriers.[32−34] Moreover, the crystal defects resulting from the lattice mismatch at the interface may accelerate ion migration and produce routes for diffusion of oxygen and moisture into the perovskite film, which may be responsible for the device degradation in an ambient environment.[35−37] To alleviate the negative effects of the interface defects on efficiency and stability of PSCs, multifarious strategies have been reported to passivate the interface defects. For example, a zwitterionic compound (3-(1-pyridinio)-1-propane sulfonate) has been applied to modify the SnO_2 film and optimize the interface, which improved device efficiency and thermal stability.[38] The $-NH_2$ group adsorbed on the surface of TiO_2 ETL has been reported to effectively passivate the defects at the interface of ETL/perovskite and decrease carrier recombination.[39] Li et al. reported a facile and effective method to passivate the defects at the interface with NH_4Cl-induced coagulated SnO_2 colloids, which obtains a PCE of 21.38%.[30] The multifunctional chemical linker 4-imidazoleacetic acid hydrochloride (Im-AcHCl) has been applied to provide a chemical bridge between the SnO_2 ETL and perovskite layer, which could passivate the interface defects and boost carrier transport.[40] These successful examples demonstrate that it is explorable to perform interface defect passivation to further improve the efficiency and stability of planar PSCs.

Here, we proposed a surface alkali-gas erosion (SAE) method to optimize SnO_2 ETL and enhance its contact with perovskite. Both the obvious chemisorption of the $-NH_2$ group on SnO_2 and crystal fusion of the SnO_2 film were observed, which were responsible to the improved electron transport, reduced interface defect states, and high-quality perovskite films. Due to the positive effects of SAE, a champion PCE of 21.10% is obtained, which is superior to that (19.04%)

https://dx.doi.org/10.1021/acsaem.0c00563
ACS Appl. Energy Mater. 2020, 3, 5039−5049

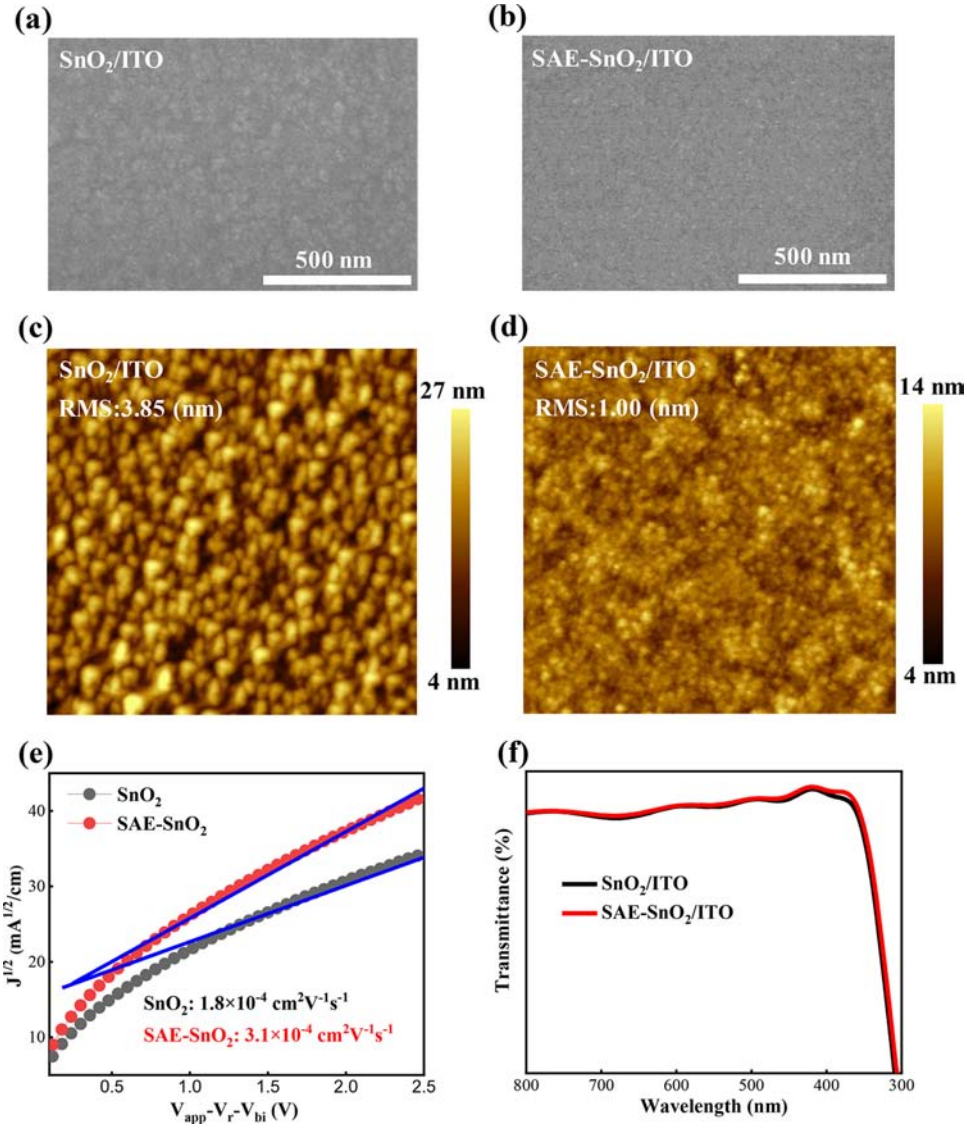

Figure 2. Characterization of ETLs, all the ETLs deposited on the ITO. (a,b) SEM images of ETLs. (c,d) AFM images of ETLs; the figure size is 2 μm. (e) Electron mobility measurement of ETLs using the SCLC model. (f) Optical transmittance spectra of ETLs.

of the control device, and a significantly improved stability is also achieved at room temperature with 40−50% humidity. It is expected that the surface alkali-gas erosion method proposed in our work is also appropriate for PSCs with large area, which may contribute to the further development of efficient and stable PSCs.

RESULTS AND DISCUSSION

In planar PSCs where the compact SnO_2 film is applied as ETL, the electronic property of ETL and its interfacial contact with perovskite strongly influence the device performance. Previous works reported that introducing the $-NH_2$ group at the ETL/perovskite interface could effectively passivate the interface defects,[39,41] and it is known that the most common and lowest-cost substance, which contains the $-NH_2$ groups, is ammonia in daily life. Theoretically speaking, the ammonia gas tends to be absorbed chemically on the surface of metal and metallic oxide.[42−45] As a kind of amphoteric oxide, SnO_2 is insoluble in alkaline solution in room temperature, however, it can be slightly dissolved when the temperature is increased. So, it is possible to simultaneously optimize the SnO_2 film chemical/physical property and introduce the $-NH_2$ group at the SnO_2/perovskite interface through erosion effects on the SnO_2 film with ammonia gas under certain conditions. Based on these theoretical thinking, we applied the surface alkali-gas erosion (SAE) method to modulate SnO_2 film features and to introduce the $-NH_2$ group on the SnO_2 surface. The detailed information of the SAE method is presented in Figure 1a. After the SnO_2 film was prepared on clean ITO, the SnO_2/ITO sample was held in a reaction chamber, which contained a certain amount of ammonia solution at the bottom, including NH_3, H_2O, and trace amounts of NH_4^+, $-NH_2$, and OH^-, and the sample was separated with the ammonia solution. Then, the chamber was heated with 120 °C for 2 h, generating alkali-gas to react with the SnO_2 film. During the SAE process, the SnO_2 film, especially the site with lots of contact points with generating gas, tends to react with OH^- ions, and the reaction equations are presented in the following:

$$SnO_2 + 2OH^- + 2NH_4^+ \leftrightarrow 2NH_4^+ - SnO_3^{2-} + H_2O \quad (1)$$

https://dx.doi.org/10.1021/acsaem.0c00563
ACS Appl. Energy Mater. 2020, 3, 5039−5049

$$2NH_4^+ - SnO_3^{2-} \leftrightarrow H_2SnO_3 \downarrow + 2NH_3\uparrow \quad (2)$$

where the $2NH_4^+-SnO_3$ is a very unstable substance and would hydrolyze to form stannic acid, a kind of sediment that is insoluble in water, as soon as it forms. Meanwhile, the $-NH_2$ group comes from ammonia solution, and the dissociation of NH_3 tends to connect with the SnO_2 because it possesses an unpaired electron that is active to connect with other dangling bonds. Previous reports reported that the $-NH_2$ group absorbed chemically on the metal oxide surface, which exhibits a stable state during the dissociation adsorption process of NH_3 on metal oxides.[42,43] The theoretical analysis indicates that the $-NH_2$ group can be absorbed steadily on the SnO_2 film.

After the SAE method was performed on the ITO/SnO_2 sample, to confirm the existence of the $-NH_2$ group on the surface of the SnO_2 film, we carried out energy-dispersive X-ray (EDS) mapping on the SnO_2 film deposited on the ITO with SAE (we named it SAE-SnO_2 in the following discussion), as shown in Figure S1, and the N element is obviously observed although the intensity of the N element is much lower than those of O and Sn elements, which suggests the existence of the $-NH_2$ group on SAE-SnO_2. In addition, the X-ray photoelectron spectroscopy (XPS) measurement was performed to further confirm the existence of the $-NH_2$ group and explore the interaction between the $-NH_2$ group and SnO_2. The original full XPS spectra of control SnO_2 and SAE-SnO_2 films are presented in Figure S2a,b, and the analysis of element content is shown in the inset table. Compared to the typical spectrum of SnO_2, the peaks of Sn 3d/O 1s/C 1s on the spectrum of SAE-SnO_2 almost share the same position and the intensities; however, it is obviously observed that the peak of N 1s arises near 400 eV. Figure 1b shows a precise map of the XPS nitrogen peak selected from the spectra of SnO_2 and SAE-SnO_2, and the peak of N 1s is clearly observed, which again confirms the existence of $-NH_2$ groups on SAE-SnO_2. The high-resolution N 1s spectrum of SAE-SnO_2 is shown in Figure 1c, which can be deconvoluted into three peaks located at 401.3, 400.6, and 399.6 eV. The peaks of 401.3 and 400.6 eV can be assigned to the γ-state including absorbed chemical N-containing species such as N−N, N−Sn, and so on, in present work, the peaks are supposed to be attributed to the N−Sn and N−H states. The peak of 399.6 eV has been reported to correspond to the $-NH_2$ moiety in previous works.[39,46] Combining the previous works and the analyses of XPS results, it is reasonable that the N element observed by the XPS measurement is in the form of $-NH_2$ absorbed on the surface of SAE-SnO_2. Comparing the Sn 3d peaks of the SnO_2 film, as shown in Figure 1d, we found that the Sn $3d_{5/2}$ (486.9 eV) and Sn $3d_{3/2}$ (495.4 eV) of the SAE-SnO_2 film shift by 0.5 eV, which may be due to the chemical interaction between the $-NH_2$ group and SnO_2 film during the SAE process.[40] The $-NH_2$ group is supposed to be absorbed on SAE-SnO_2 through the N-Sn bond, which is consistent with the discussion of the peak of N 1s centered at 401.3 and 400.6 eV mentioned above. After SAE was applied on the SnO_2 film, we heated the sample of ITO/SAE-SnO_2 for 20 min with 50, 100, and 150 °C (higher than the annealing temperature (130 °C) of the perovskite film), and then XPS was carried out on them. As shown in Figure S2c, it is clear to see that the intensity of the N 1s peak changed negligibly with different heating temperatures, which further confirms the chemical interaction between the $-NH_2$ group and SnO_2 film and rules out the possibility of the $-NH_2$ group being absorbed physically. All these results of various measurements verified that the SAE method can successfully introduce the $-NH_2$ group on the surface of SnO_2 ETL.

To understand the effects of surface alkali-gas erosion (SAE) on the surface morphology of the SnO_2 film, scanning electron microscopy (SEM) was carried out on control SnO_2 and SAE-SnO_2 films. As shown in Figure 2a,b, both films are compact without cavities and pinholes. However, observing Figure 2a in detail, we found a lot of aggregate structures located chaotically on the surface. Compared to the control SnO_2 film, the SAE-SnO_2 film has a smoother and flatter surface with crystal fusion, which looks like being polished due to the erosion effects of SAE. To understand the morphology difference more accurately and get a clear value of surface roughness, atomic force microscopy (AFM) was carried out, and the results are shown in Figure 2c,d, respectively. In Figure 2c, the control SnO_2 film is compact, and the grains have a disorder arrangement with an obvious boundary. Compared to the control SnO_2 film, the SAE-SnO_2 film exhibits a smoother surface, and the RMS is 1.00 nm, which is lower than that (3.85 nm) of the control SnO_2 film. We can find that all the grains fuse together, which obfuscates the grain boundary. Due to the decreased roughness and boundary, the SAE-SnO_2 film may significantly decrease the surface defect states and facilitate the deposition of high-quality perovskite films. We also performed Kelvin probe force microscopy (KPFM) on control SnO_2 and SAE-SnO_2 films with the resulting images shown in Figure S3. We found that the surface potential distribution is in accordance with the surface morphology mentioned above, and the average potential of SAE-SnO_2 film is −120 mV that is inferior to that (180 mV) of the control SnO_2 film, which explains why the SAE-SnO_2 film possesses a lower Fermi-level, indicating a better band alignment with perovskite.[6,28,47]

In addition, to measure the electron mobility of control SnO_2 and SAE-SnO_2 films, the space charge-limited current (SCLC) was measured with the device structure of ITO/Au/ETL/Au.[48] As shown in Figure 2e, we calculate the electron mobility of the SAE-SnO_2 film to be 3.1×10^{-4} cm^2 V^{-1} S^{-1}, which is obviously higher than that (1.8×10^{-4} cm^2 V^{-1} S^{-1}) of the SnO_2 film, according to the following Mott−Gurney function:

$$\mu_s = \frac{8jL^3}{9\varepsilon_0\varepsilon(V_{app} - V_r - V_{bi})^2} \quad (3)$$

where j is the current density, L is the thickness of the ETL, ε_0 is the vacuum permittivity, ε is the relative dielectric constant of ETL, V_{app} is the applied voltage, V_r is the voltage loss due to radiative recombination, and V_{bi} is the built-in voltage due to the different work functions between the anode and cathode. It is known that the increased electron mobility effectively promotes the carrier transport in the PSCs and decreases the charge accumulation at the ETL/perovskite interface. The conductivities of control SnO_2 and SAE-SnO_2 films were also measured with the results shown in Figure S4a, and the device structure is presented in the inset figure. We found that the resistance of the SAE-SnO_2 film is apparently smaller than that of the SnO_2 film, which may be due to the smoother surface and surface crystal fusion mentioned above. The crystallization properties of control SnO_2 and SAE-SnO_2 films were explored by X-ray diffraction (XRD) measurement, as shown in Figure

https://dx.doi.org/10.1021/acsaem.0c00563
ACS Appl. Energy Mater. 2020, 3, 5039−5049

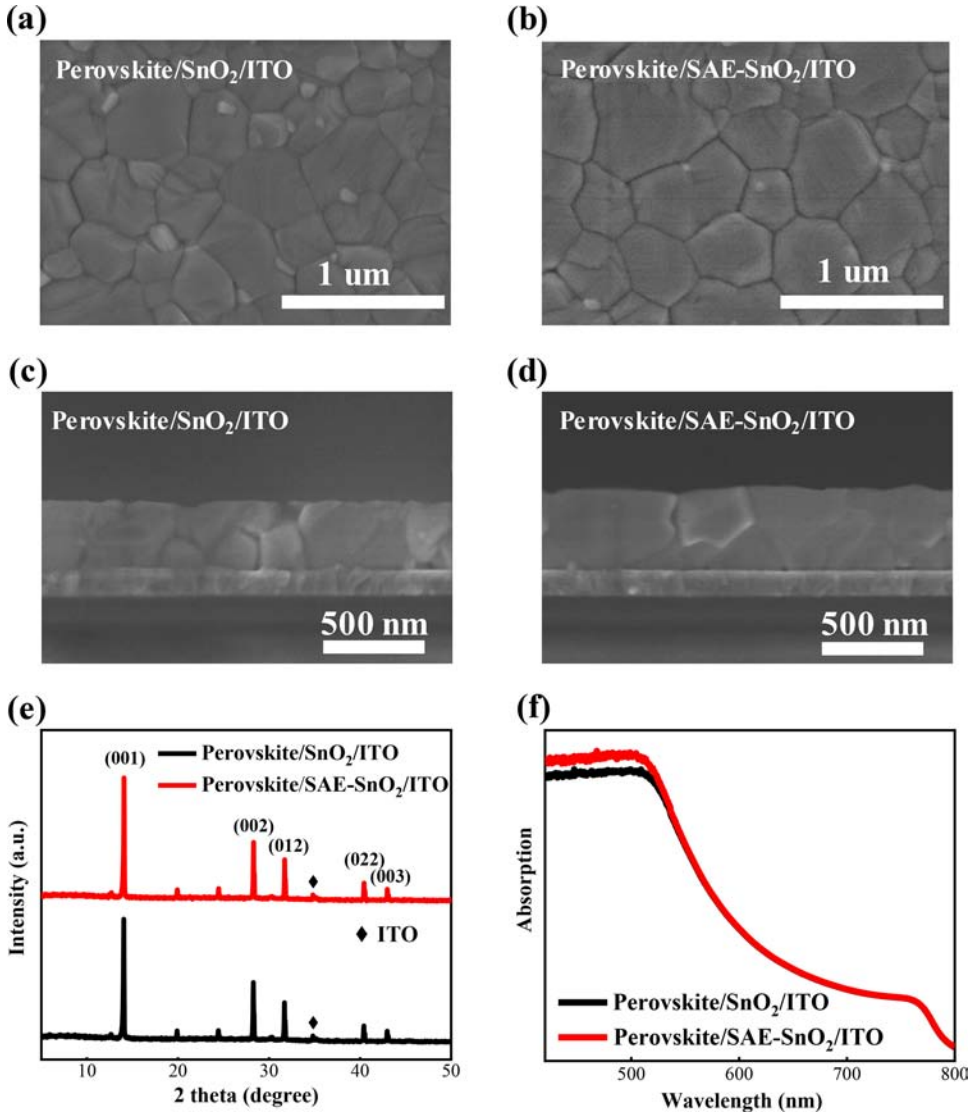

Figure 3. Characterization of the perovskite films. (a) Top-view SEM image of the perovskite film. (b) Top-view SEM image of the perovskite film. (c) Cross-sectional SEM image of the perovskite film. (d) Cross-sectional SEM image of the perovskite film. (e) XRD patterns of the perovskite films. (f) UV−vis absorption spectra of the perovskite films.

S4b; the XRD peaks of control SnO_2 and SAE-SnO_2 films are similar, and all of them are indexed to the typical diffraction peaks of the SnO_2 film. The transmittance is a key factor for ETL applied in planar n-i-p PSCs; after SAE was applied on the SnO_2 film, the UV−vis absorption measurement was carried out on control SnO_2 and SAE-SnO_2 films. As shown in Figure 2f, the two films exhibit outstanding transmittance in the range of 300 to 800 nm wavelengths, and the transmittance of the SAE-SnO_2 film is slightly superior to that of the SnO_2 film, indicating that the SAE process has beneficial effects on the ETL transmittance and would not pollute and stain the ITO/SnO_2 samples, which demonstrated that the SAE method is suitable for the fabrication of planar n-i-p PSCs.

After surface alkali-gas erosion (SAE) was performed on SnO_2, it is necessary to explore its impacts on the perovskite film since the perovskite film is deposited on the SnO_2 film directly, and the micromorphology of the substrate has a huge influence on the perovskite film, including surface coverage, grain size, crystalline, and so on. Figure 3 illustrates the SEM images, XRD patterns, and UV−vis absorption spectra of the perovskite film deposited on the SnO_2/ITO substrate without/with SAE (we name them the control perovskite film and perovskite film on SAE-SnO_2, respectively, in the following discussion). First, we analyze the perovskite film surface micromorphology from the SEM images. In Figure 3a, the control perovskite film is compact without pinholes, and the average grain size is about 350 nm, we found that the film surface is bestrewed with a fragmentary crystal, which is small and arranged randomly. In comparison, as shown in Figure 3b, the perovskite film on SAE-SnO_2 is compact with uniform grains, and the average size of grains is about 550 nm, in detail, there is a negligible fragmentary grain located on the grain surface and at the grain boundary. In addition, AFM was also used to analyze the morphology of the perovskite film. As shown in Figure S5a and Figure 5b, both films are compact, and the RMS of the perovskite film on SAE-SnO_2 is 14.61 nm, which is slightly smaller than that (16.36 nm) of the control perovskite film. Besides the observation of the surface morphology, we also observed the cross-sectional image to further analyze the crystal quality of the perovskite film. As

https://dx.doi.org/10.1021/acsaem.0c00563
ACS Appl. Energy Mater. 2020, 3, 5039−5049

shown in Figure 3c, the thickness of the control perovskite film is about 500 nm, and the grain orientation is disordered with obvious grain boundaries. In comparison, as shown in Figure 3d, the thickness of the perovskite film on SAE-SnO_2 is about 600 nm, and almost all the grains penetrate the whole film with an orientation vertical to the substrate. The grains are obviously larger than that of the control perovskite film, which is in agreement with the results of SEM measurement discussed above.

Moreover, the chemical compositions and crystal structures of perovskite films are explored by XRD measurement. As shown in Figure 3e, the crystal faces corresponding to different peak positions are labeled, and we found that both perovskite films exhibit similar peak positions, indexed to the typical diffraction peaks of a perovskite. The peak intensity of the perovskite film on SAE-SnO_2 is slightly higher than that of the control perovskite film, indicating a higher crystallization quality. From the optical perspective, as shown in Figure 3f, the perovskite film on SAE-SnO_2 exhibits a stronger absorption especially in the range of 400 to 550 nm compared to the control perovskite film, which is helpful to light capture of PSCs and further to obtain high current density. All the results discussed show that the crystallization quality of the perovskite film is enhanced after the SAE method has been applied on SnO_2 ETL. There may be two main reasons: the first one is, as shown in Figure 4, that the $-NH_2$ groups absorbed on the

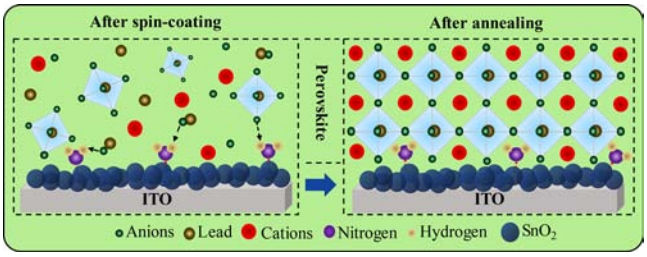

Figure 4. Schematic structure and nucleation process at perovskite/ETL interfaces.

SAE-SnO_2 surface would strongly interact with the halide anions of perovskite through hydrogen bonds,[49] which can provide nucleation sites for promoting perovskite crystal nucleation via accelerating the atoms in preheating the perovskite film assembled together. Based on classical nucleation theory, during the nucleation process, the reduction of volume free energy due to the decreased temperature can only compensate for 2/3 of the surface energy of the nucleus, and the rest of the surface energy needs to be supplied by the circumstance that mainly comes from the local energy fluctuation in the preheating perovskite film. The existence of hydrogen bonds formed between the halide anions of perovskite and $-NH_2$ group could effectively increase local energy fluctuation and further to accelerate crystal nucleation. In addition, the $-NH_2$ groups possess a smaller molecular dimension than the organic molecular of perovskite, such an advantage helps it to move into the perovskite inorganic framework and replace the organic molecular at the bottom perovskite film with the annealing process proceeding, which can also accelerate the perovskite crystal nucleation and bridge-link with SAE-SnO_2 and perovskite.[50,51] The second one may be attributed to the optimized micromorphology of SAE-SnO_2 that can further obtain a high-quality perovskite film.

The interfacial property is expected to be optimized after surface alkali-gas erosion (SAE) was applied on SnO_2, and we performed various measurements to explore the influence of the SAE method on the perovskite/ETL interfacial charge transfer and interface defect states, including the PL and TRPL, the dark $J-V$ curves, electrochemical impedance spectroscopy (EIS), and so on. As shown in Figure S6a, compared to the steady-state PL spectrum of the control perovskite film, the steady-state PL spectrum of the perovskite film on SAE-SnO_2 shows an obvious PL quenching, which means that the carriers extracted from the perovskite film through the ETL have increased, indicating that the SAE process effectively enhances the capability of SnO_2 for electron extraction. The results of TRPL measurement are shown in Figure S6b. The specific value of the decay lifetime is estimated by fitting the TRPL spectral curves and shown in the inset in Figure S6b. We found that the fast decay lifetime $\tau 1$ (74 ns) of the perovskite film on SAE-SnO_2 is almost half of that (142 ns) of the control perovskite film, indicating that the carriers are extracted effectively at the interface of perovskite/SAE-SnO_2, which is consistent with the result of the PL measurement. The carrier transfer improved at the perovskite/SAE-SnO_2 interface may have two reasons: the first one is that the $-NH_2$ groups absorbed chemically on the SnO_2 build an available bridge-link between perovskite and SnO_2, which strengthens the interface contact and perovskite/ETL interface charge transfer.[30] The second one is that the improved carrier mobility of SAE-SnO_2 can promote carrier extraction obviously. Compared to the slow decay lifetime $\tau 2$ (174 ns) of the control perovskite film, the $\tau 2$ (181 ns) of the perovskite film on SAE-SnO_2 is prolonged, mainly due to the decreased trap-assisted recombination in the perovskite film, indicating a higher crystallization quality that is consistent with the results of SEM and XRD tests.

The devices for dark $J-V$ curves and EIS measurements are structured as ITO/SnO_2(SAE-SnO_2)/$FA_{0.15}MA_{0.85}PbI_3$/Spiro-OMeTAD/Au, and the cross-sectional SEM image of the device with SAE-SnO_2 is shown in Figure 5a, where the $-NH_2$ groups absorbed on the SAE-SnO_2 film tend to replace the organic molecules in the bottom perovskite film. We found that the perovskite film possesses a good crystallinity, and the grains almost penetrate the full film, which is consistent with the results of the cross-sectional SEM images of the perovskite film mentioned above.

The dark-curve measurement was performed to further verify the charge-carrier dynamic and carrier recombination in the device with SAE-SnO_2 or SnO_2. As shown in Figure 5b, the current density of the device with SAE-SnO_2 is almost 2 orders of magnitude lower than that of the device with SnO_2. This result manifests that more photon-generated carriers are transported through the charge transport layer in the device with SAE-SnO_2, which indicates that the SAE-SnO_2 as ETL can suppress the interfacial carrier recombination obviously. In addition, we fabricated the electron-only device with the architecture (ITO/ETL/Perovskite/PCBM/Au) shown in the inset of Figure 5c to quantitatively evaluate the trap density of the devices with SAE-SnO_2 and SnO_2.[40,52] The dark $J-V$ curves of the electron-only devices are shown in Figure 5c, and the trap density (N_{trap}) is determined by the equation:

$$N_{trap} = \frac{2\varepsilon_0 \varepsilon V_{TFL}}{eL^2} \quad (4)$$

https://dx.doi.org/10.1021/acsaem.0c00563
ACS Appl. Energy Mater. 2020, 3, 5039−5049

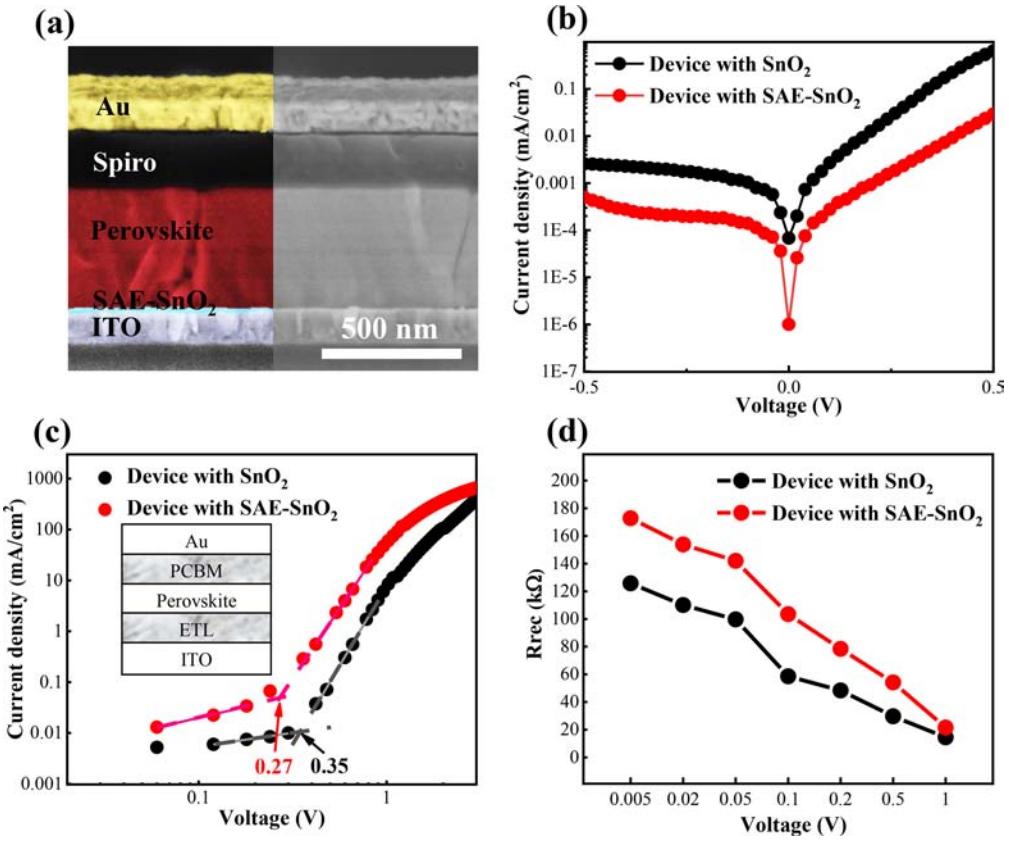

Figure 5. Charge transfer and defect states at perovskite/ETL interfaces in the devices. (a) The cross-sectional SEM image of the device with SAE-SnO_2. (b) Dark $J-V$ curves. (c) Dark $J-V$ curves of electron-only devices. (d) R_{rec} of the corresponding device under different applied voltages.

where ε_0 is the vacuum permittivity, ε is the relative dielectric constant of perovskite, V_{TFL} is the trap-field limit voltage, e is the electron charge, and L is the thickness of the perovskite film. N_{trap} is linearly dependent on V_{TFL} due to the two devices sharing the same ε_0, ε, e, and L. As shown in Figure 5c, the device with SAE-SnO_2 presents a much smaller V_{TFL} (0.27 V) than that with SnO_2 (0.35 V), which indicates that SAE-SnO_2 can decrease the defect states effectively. The decreased trap density may be attributed to the smooth morphology with crystal fusion of the SnO_2 film and $-NH_2$ groups absorbed on the SnO_2, which obtains a high-quality crystalline perovskite film and passivation of defect states at the ETL/perovskite interface. Besides the dark-curve measurement, we also performed electrochemical impedance spectroscopy (EIS) to investigate the interfacial charge transport properties in the device. The Nyquist plots of devices with different ETLs were measured in the dark circumstance in the frequency range of 1 Hz to 1 MHz under a series of reverse potentials including 0.005, 0.02, 0.05, 0.01, 0.2, 0.5, and 1 V, and all the reverse potentials were smaller than the open-circuit voltage of the device. As shown in Figure S7, the Nyquist plots are measured under a reverse potential of 0.5 V, and the corresponding fitted curves based on the equivalent circuit model are also presented in the inset figure. From the high-frequency region of the fitting curves representing the charge recombination process, we found that R_{rec} (recombination resistant) (29.69 KΩ) extracted from the fitting curves of the device with SnO_2 is much smaller than that (54.19 KΩ) of the device with SAE-SnO_2. R_{rec} under different reverse potentials are displayed in Figure 5d, R_{rec} data under different voltages are summarized in Table S1. From the results, we found that, with reverse potential increasing, both R_{rec} values of the device with SAE-SnO_2 or SnO_2 exhibit a similar variation trend, however, no matter the reverse potential is, under the same bias, the device with SAE-SnO_2 exhibits a larger R_{rec} than that with SnO_2. All the results of the EIS test demonstrate suppressed charge-recombination owing to the effective passivation of defect states in the device with SAE-SnO_2, which is consistent with the discussion of the dark-curve measurements.

The above results and discussion suggest that the surface alkali-gas erosion (SAE) can effectively optimize SnO_2 films and decrease trap-assisted recombination in the PSCs, indicating its potential to obtain efficient and stable PSCs. To explore the influence of the SAE process on performance of PSCs, we fabricated the $FA_{0.15}MA_{0.85}PbI_3$-based PSCs with SAE-SnO_2 and SnO_2 as the ETLs and collected the short-circuit current density (J_{SC}), open-circuit voltage (V_{OC}), fill factor (FF), and photoelectric conversion efficiency (PCE) of the devices. First, we investigated the effects of treatment time of SAE on PSC performance. Figure S8a shows the $J-V$ curves of PSCs with different treatment times, and the statistic parameters are listed in the inset table. It is obviously found that the device with the highest PCE is obtained with 2 h. Hereafter, the data of PSCs with SAE-SnO_2 are based on the SAE with 2 h. We also investigated the effects of concentration of NH_3-H_2O solution put into the chamber for SAE on PSC performance. The $J-V$ curves of PSCs with different dilution rates of NH_3-H_2O solution are presented in Figure S8b, and the statistic parameters are listed in Table S2. We found that the device with the highest PCE is obtained with NH_3-H_2O solution without dilution; hereafter, the data of PSCs with SAE-SnO_2 are based on the condition of original NH_3-H_2O

https://dx.doi.org/10.1021/acsaem.0c00563
ACS Appl. Energy Mater. 2020, 3, 5039−5049

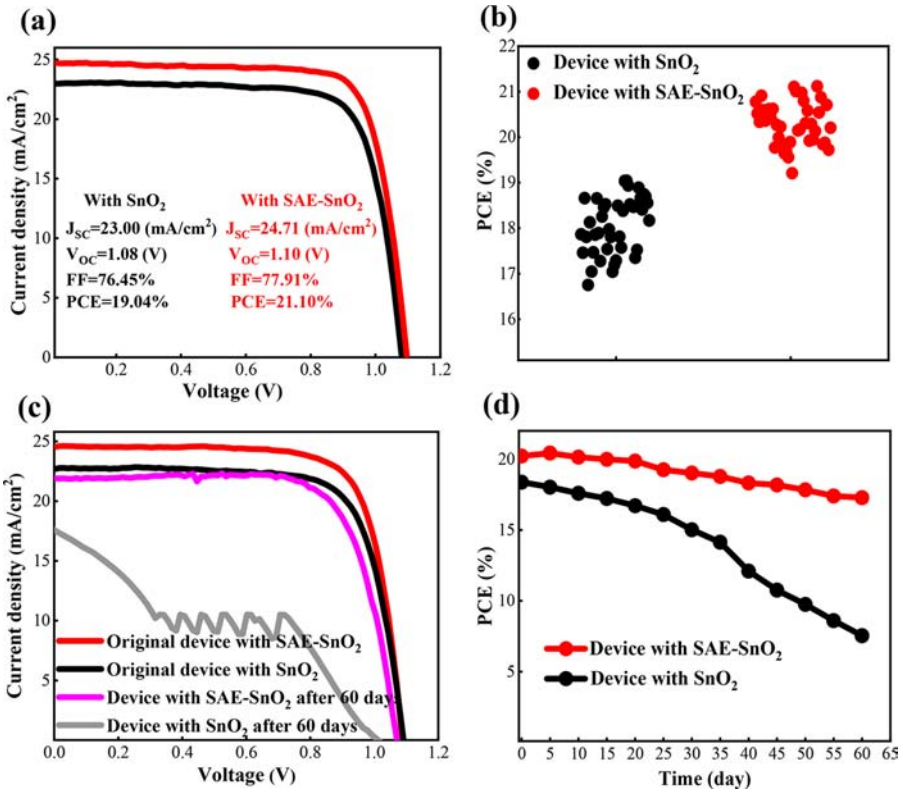

Figure 6. Device performance with different ETLs. (a) $J-V$ curves of devices. (b) The PCE distribution of 40 devices. (c) $J-V$ curves of devices before and after aging tests. (d) Long-term stability of devices.

solution without dilution. We selected the champion PCE of the PSCs with SAE-SnO_2 and SnO_2, as shown in Figure 6a. The champion PCE of PSCs with SAE-SnO_2 is 21.10%, 10.82% higher than that (19.04%) of PSCs with SnO_2. The J_{SC} (24.71 mA cm^{-2}) of PSCs with SAE-SnO_2 is 7.4% higher than that (23.00 mA cm^{-2}) of PSCs with SnO_2, which is improved obviously as expected. Furthermore, to demonstrate the reproducibility of PSCs with SAE-SnO_2, we gathered performance statistics of 40 PSCs with SAE-SnO_2 and SnO_2. The distribution of PCE is presented in Figure 5b, and the distribution of J_{SC}, V_{OC}, and FF is displayed in Figure S8c−e, respectively. It is obviously observed that the PSCs with SAE-SnO_2 show a better performance and reproducibility than the PSCs with SnO_2, which may due to the optimized SnO_2 film and suppressed trap-assisted recombination after the SAE method. The PCE of the PSCs with SnO_2 is widely distributed in the range of 16.75 to 19.04%, and the average PCE is 18.07%; J_{SC} is distributed in the range of 20.83 to 23.52 mA cm^{-2}, and the average is 22.34 mA cm^{-2}. In comparison, the PCE of the PSCs with SAE-SnO_2 is distributed in a narrower range of 19.21 to 21.10%, and the average PCE is 20.30%, which is much higher. The improved PCE mainly results from the improvement of J_{SC} that the average value of PSCs with SAE-SnO_2 is 24.19 mA cm^{-2}, which is apparently higher than that (22.34 mA cm^{-2}) of PSCs with SnO_2. The FF of the device with SAE-SnO_2 is 76.89%, which is also improved due to the optimized interface contacts.

We also explored the effects of SAE on hysteresis of PSCs, as shown in Figure S8f and Table S3, and we found that the hysteresis of PSCs with SAE-SnO_2 gets mitigated obviously compared to PSCs with SnO_2, mainly due to the reduced trap-induced carrier recombination and balanced charge-carrier transport.[53,54] It is well known that the interfacial contact and interface defect states play a key role in determining the stability of PSCs. Here, the stability of unencapsulated PSCs (ITO/SnO_2(SAE-SnO_2)/Perovskite/Spiro-OMeTAD/Au) stored for 60 days in an ambient condition with 40−50% humidity at room temperature in the dark was compared. The $J-V$ curves of devices before and after aging tests are presented in Figure 6c, and Table 1 displays the statistic parameters of

Table 1. Parameters of Device Performance

device	J_{SC} (mA cm^{-2})	V_{OC} (V)	FF (%)	PCE (%)
with SAE-SnO_2; original	24.55	1.083	76.06	20.22
with SAE-SnO_2; after 60 days	21.91	1.070	73.72	17.28
with SnO_2; original	22.71	1.096	73.84	18.38
with SnO_2; after 60 days	17.51	1.018	42.32	7.54

the devices. We found that the PSCs with SAE-SnO_2 obviously exhibit a better stability, especially reflected in the FF and PCE. To further monitor the change of device performance, we recorded the parameters of the device every 5 days. The change of PCE is shown in Figure 5d, and the changes of J_{SC}, V_{OC}, and FF are displayed in Figure S9a−c, respectively. We found that the PSCs with SAE-SnO_2 retain 86% of its initial PCE after 60 days, while the PSCs with SnO_2 retain only 41% of its initial PCE. In detail, the FF decline is also elevated effectively with the SAE method after 60 days. The PSCs with SAE-SnO_2 maintain 95% of its initial FF, while the PSCs with SnO_2 maintain only 57% of its initial FF. There may be two main reasons for the improved stability: first, the polished SnO_2 and bridge-linked ETL/perovskite interface enhanced the interface contacts and reduced interface defects, which

https://dx.doi.org/10.1021/acsaem.0c00563
ACS Appl. Energy Mater. 2020, 3, 5039−5049

effectively inhibited the ion migration and hindered diffusion of oxygen and moisture into the perovskite film. Second, the introduction of the $-NH_2$ group improved the crystallinity of the perovskite film, reduced the defect state in the perovskite film, and further enhanced its inherent stability.

CONCLUSIONS

In summary, a dual functional surface alkali-gas erosion (SAE) method was proposed to optimize electronic properties and interface contact with perovskite of the SnO_2 film through ammonia erosion under a certain condition. We elucidated the chemical reaction mechanism between SnO_2 and alkaline gas during the SAE method and confirmed that the SnO_2 film surface is polished effectively, and the electron mobility is improved. Meanwhile, the $-NH_2$ group absorbed chemically on the SnO_2 surface through the SAE method was demonstrated could promote ETL/perovskite interfacial transport and improve the crystallinity of the perovskite film. By employing the SAE method, the high-efficiency PSCs can lead to a champion PCE over 21% with distinctly improved device stability. Our work provides an available method to effectively optimize ETL toward efficient and stable PSCs, and we believe that the SAE method is suitable for any other ETLs based on the amphoteric oxide, including TiO_2, ZnO, and Al_2O_3, and we also believe that the SAE method is also appropriate for PSCs with large area and other optoelectronic applications, such as light-emitting diodes and photodetectors.

EXPERIMENTAL PROCEDURES

Device Fabrication. *Solution Preparation.* To prepare SnO_2 solution, the SnO_2 colloid precursor (Alfa) was diluted with deionized water with a volume ratio of 1:5 and stirred lightly. To prepare perovskite precursor solution, 0.15 *m* FAI, 0.85 *m* MAI, and 1.025 *m* PbI_2 were mixed in anhydrous dimethylformamide/dimethyl sulfoxide (600/78 mg) solution, which was stirred for 4 h at room temperature in the glove box. To prepare the HTM precursor, Spiro-OMeTAD was dissolved in chlorobenzene with a concentration of 80 mg mL^{-1}, and then *tert*-butylpyridine (28.5 μL in 1 mL chlorobenzene) and lithium bis(trifluoromethanesulfonyl) imide (8.75 mg mL^{-1}) were added into the Spiro-OMeTAD solution as the additives, which was stirred in the glove box for 6 h.

Perovskite Solar Cell Fabrication. ITO glass (10 Ω $sq.^{-1}$) was ultrasonically cleaned sequentially with detergent solution, deionized water, acetone, ethyl alcohol, and deionized water for 20 min. After drying, these clean substrates were treated with UV-ozone for 20 min before using. The SnO_2 film was fabricated by spin-coating with prepared precure solution at 4000 rpm for 15 s followed by heating at 150 °C for 30 min. After the SnO_2 film was prepared, the SnO_2/ITO sample was held in a reaction chamber containing a certain amount of ammonia solution, and the sample was separated with the ammonia solution. Then, the chamber was sealed and heated with 120 °C for 2 h, generating alkali-gas to react with the SnO_2 film; after heating, the SnO_2/ITO sample was taken out, washed with deionized water and ethyl alcohol, and then dried for the next step. The SnO_2 film was further treated with UV-ozone for 15 min after it was cooled down to room temperature and then transferred into the N_2-filled glove box. To fabricate the perovskite film, the perovskite precursor was spin-coated on the SnO_2 substrate at 4000 rpm for 25 s. During the spin-coating step, 0.8 mL of diethyl ether was poured on the surface at 18 s before the end. The prepared film was heated at 130 °C for 15 min and then cooled to room temperature naturally. Then the Spiro-OMeTAD solution was spin-coated at 4000 rpm for 30 s on the perovskite films. Finally, the 60 nm Au electrode was evaporated on the film.

Device Characterization. To explore the performance of the PSCs, current−voltage curves were measured using a source meter (Keithley 2400) under AM 1.5G irradiation with a power density of 100 mW cm^{-2} from a solar simulator (XES-301S + EL-100) by forward (−0.1 to 1.2 V) or reverse (1.2 to −0.1 V) scans. The light intensity was calibrated with an NIM-certified Si reference cell. The step voltage was fixed at 12 mV, and the delay time was set at 10 ms. All PSCs were fabricated with a metal mask that was used to define the active area, which is 0.1 cm^2. To confirm the existence of the N element on the SAE-SnO_2 film, XPS measurement was performed, and XPS spectra were collected using a Thermo Fisher Scientific ESCALAB 250Xi under 10^{-9} torr vacuum using a monochromic Al Kα X-ray source. All spectra were shifted to account for sample charging using inorganic Au as reference. The morphologies of SnO_2 and perovskite films were characterized by scanning electron microscopy (SEM) (FEI SIRION 200) and atomic force microscopy (AFM) (Agilent Keysight AFM-5500). The chemical compositions and structures of the SnO_2 and perovskite films were analyzed by X-ray diffraction (XRD) (Bruker D8 Advance X-ray diffractometer, Cu Kα radiation λ = 0.15406 nm). The steady-state PL spectra of the perovskite films were measured by a spectrometer (Edinburgh PLS 980) at 80 K. The absorption spectra of perovskite films were measured by a UV−vis spectrophotometer (UV-2600). The EIS patterns of the PSCs were measured by an electrochemical workstation (Zahner Zennium).

ASSOCIATED CONTENT

Supporting Information

The Supporting Information is available free of charge at https://pubs.acs.org/doi/10.1021/acsaem.0c00563.

SEM image and EDS mapping of the SAE-SnO_2 film, characterization of the ETLs, characterization of the perovskite films, the charge transfer between perovskite and different ETLs, EIS spectra of devices, and performances of devices (PDF)

AUTHOR INFORMATION

Corresponding Author

Meicheng Li − *State Key Laboratory of Alternate Electrical Power System with Renewable Energy Sources, School of Renewable Energy, North China Electric Power University, Beijing 102206, China;* orcid.org/0000-0002-0731-741X; Email: mcli@ncepu.edu.cn

Authors

Hao Huang − *State Key Laboratory of Alternate Electrical Power System with Renewable Energy Sources, School of Renewable Energy, North China Electric Power University, Beijing 102206, China*

Xin Liu − *State Key Laboratory of Alternate Electrical Power System with Renewable Energy Sources, School of Renewable Energy, North China Electric Power University, Beijing 102206, China*

Mingjun Duan − *State Key Laboratory of Alternate Electrical Power System with Renewable Energy Sources, School of Renewable Energy, North China Electric Power University, Beijing 102206, China*

Jun Ji − *State Key Laboratory of Alternate Electrical Power System with Renewable Energy Sources, School of Renewable Energy, North China Electric Power University, Beijing 102206, China*

Haoran Jiang − *State Key Laboratory of Alternate Electrical Power System with Renewable Energy Sources, School of Renewable Energy, North China Electric Power University, Beijing 102206, China*

Benyu Liu − *State Key Laboratory of Alternate Electrical Power System with Renewable Energy Sources, School of Renewable*

https://dx.doi.org/10.1021/acsaem.0c00563
ACS Appl. Energy Mater. 2020, 3, 5039−5049

Energy, North China Electric Power University, Beijing 102206, China

Sajid Sajid − *State Key Laboratory of Alternate Electrical Power System with Renewable Energy Sources, School of Renewable Energy, North China Electric Power University, Beijing 102206, China*

Peng Cui − *State Key Laboratory of Alternate Electrical Power System with Renewable Energy Sources, School of Renewable Energy, North China Electric Power University, Beijing 102206, China*

Dong Wei − *State Key Laboratory of Alternate Electrical Power System with Renewable Energy Sources, School of Renewable Energy, North China Electric Power University, Beijing 102206, China*

Yingfeng Li − *State Key Laboratory of Alternate Electrical Power System with Renewable Energy Sources, School of Renewable Energy, North China Electric Power University, Beijing 102206, China*

Complete contact information is available at: https://pubs.acs.org/10.1021/acsaem.0c00563

Author Contributions

‡H.H. and X.L. contributed equally. The manuscript was written through contributions of all authors. All authors have given approval to the final version of the manuscript.

Notes

The authors declare no competing financial interest.

■ ACKNOWLEDGMENTS

This work is supported partially by National Natural Science Foundation of China (Grant nos. 51772096 and 51972110), Beijing Science and Technology Project (Z181100005118002), Par-Eu Scholars Program, Science and Technology Beijing 100 Leading Talent Training Project, the Fundamental Research Funds for the Central Universities (2017ZZD02), and the NCEPU "Double First-Class" Graduate Talent Cultivation Program.

■ REFERENCES

(1) Kojima, A.; Teshima, K.; Shirai, Y.; Miyasaka, T. Organometal Halide Perovskites as Visible-light Sensitizers for Photovoltaic cells. *J. Am. Chem. Soc.* **2009**, *131*, 6050−6051.

(2) Luo, D.; Yang, W.; Wang, Z.; Sadhanala, A.; Hu, Q.; Su, R.; Shivanna, R.; Trindade, G. F.; Watts, J. F.; Xu, Z.; Liu, T.; Chen, K.; Ye, F.; Wu, P.; Zhao, L.; Wu, J.; Tu, Y.; Zhang, Y.; Yang, X.; Zhang, W.; Friend, R. H.; Gong, Q.; Snaith, H. J.; Zhu, R. Enhanced Photovoltage for Inverted Planar Heterojunction Perovskite Solar Cells. *Science* **2018**, *360*, 1442−1446.

(3) Wei, D.; Ma, F.; Wang, R.; Dou, S.; Cui, P.; Huang, H.; Ji, J.; Jia, E.; Jia, X.; Sajid, S.; Elseman, A. M.; Chu, L.; Li, Y.; Jiang, B.; Qiao, J.; Yuan, Y.; Li, M. Ion-Migration Inhibition by the Cation-π Interaction in Perovskite Materials for Efficient and Stable Perovskite Solar Cells. *Adv. Mater.* **2018**, *30*, 1707583.

(4) Kim, J.; Ho-Baillie, A.; Huang, S. Review of Novel Passivation Techniques for Efficient and Stable Perovskite Solar Cells. *Sol. RRL* **2019**, *3*, 1800302.

(5) Wei, D.; Ji, J.; Song, D.; Li, M.; Cui, P.; Li, Y.; Mbengue, J. M.; Zhou, W.; Ning, Z.; Park, N.-G. A TiO_2 Embedded Structure for Perovskite Solar Cells with Anomalous Grain Growth and Effective Electron Extraction. *J. Mater. Chem. A* **2017**, *5*, 1406.

(6) Cui, P.; Wei, D.; Ji, J.; Huang, H.; Jia, E.; Dou, S.; Wang, T.; Wang, W.; Li, M. Planar p-n Homojunction Perovskite Solar Cells with Efficiency Exceeding 21.3%. *Nat. Energy* **2019**, *4*, 150−159.

(7) Jiang, L.-L.; Wang, Z.-K.; Li, M.; Li, C.-H.; Fang, P.-F.; Liao, L. S. Enhanced Electrical Property of Compact TiO_2 Layer via Platinum Doping for High-Performance Perovskite Solar Cells. *Sol. RRL* **2018**, *2*, 1800149.

(8) Jiang, Q.; Zhang, L.; Wang, H.; Yang, X.; Meng, J.; Liu, H.; Yin, Z.; Wu, J.; Zhang, X.; You, J. Enhanced Electron Extraction Using SnO_2 for High-efficiency Planar-Structure $HC(NH_2)_2PbI_3$-based Perovskite Solar Cells. *Nat. Energy* **2017**, *2*, 16177.

(9) Jiang, Q.; Zhao, Y.; Zhang, X.; Yang, X.; Chen, Y.; Chu, Z.; Ye, Q.; Li, X.; Yin, Z.; You, J. Surface Passivation of Perovskite Film for Efficient Solar Cells. *Nat. Photonics* **2019**, *13*, 460−466.

(10) Heo, J. H.; Lee, M. H.; Han, H. J.; Patil, B. R.; Yu, J. S.; Im, S. H. Highly Efficient Low Temperature Solution Processable Planar Type $CH_3NH_3PbI_3$ Perovskite Flexible Solar Cells. *J. Mater. Chem. A* **2016**, *4*, 1572−1578.

(11) Jiang, Q.; Zhang, X.; You, J. SnO2 : A Wonderful Electron Transport Layer for Perovskite Solar Cells. *Small* **2018**, *14*, 1801154.

(12) Song, S.; Kang, G.; Pyeon, L.; Lim, C.; Lee, G. Y.; Park, T.; Choi, J. Systematically Optimized Bilayered Electron Transport Layer for Highly Efficient Planar Perovskite Solar Cells (η = 21.1%). *ACS Energy Lett.* **2017**, *2*, 2667−2673.

(13) Ke, W.; Fang, G.; Liu, Q.; Xiong, L.; Qin, P.; Tao, H.; Wang, J.; Lei, H.; Li, B.; Wan, J.; Yang, G.; Yan, Y. Low-temperature Solution-processed Tin Oxide as an Alternative ElectronTransporting Layer for Efficient Perovskite Solar Cells. *J. Am. Chem. Soc.* **2015**, *137*, 6730−6733.

(14) Wei, D.; Huang, H.; Cui, P.; Ji, J.; Dou, S.; Jia, E.; Sajid, S.; Cui, M.; Chu, L.; Li, Y.; Jiang, B.; Li, M. Moisture-tolerant Supermolecule for The Stability Enhancement of Organic-inorganic Perovskite Solar Cells in Ambient Air. *Nanoscale* **2019**, *11*, 1228−1235.

(15) Yang, X.; Zhang, X.; Deng, J.; Chu, Z.; Jiang, Q.; Meng, J.; Wang, P.; Zhang, L.; Yin, Z.; You, J. Efficient Green Light-emitting Diodes Based on Quasi-two-dimensional Composition and Phase Engineered Perovskite with Surface Passivation. *Nat. Commun.* **2018**, *9*, 570.

(16) Anaraki, E. H.; Kermanpur, A.; Steier, L.; Domanski, K.; Matsui, T.; Tress, W.; Saliba, M.; Abate, A.; Grätzel, M.; Hagfeldt, A.; Correa-Baena, J.-P. Highly Efficient and Stable Planar Perovskite Solar Cells by Solution-processed Tin Oxide. *Energy Environ. Sci.* **2016**, *9*, 3128−3134.

(17) Bu, T.; Liu, X.; Zhou, Y.; Yi, J.; Huang, X.; Luo, L.; Xiao, J.; Ku, Z.; Peng, Y.; Huang, F.; Cheng, Y.-B.; Zhong, J. A Novel Quadruple-cation Absorber for Universal Hysteresis Elimination for High Efficiency and Stable Perovskite Solar Cells. *Energy Environ. Sci.* **2017**, *10*, 2509−2515.

(18) Nguyen, N. M.; Luu, M. Q.; Nguyen, M. H.; Nguyen, D. T.; Bui, V. D.; Truong, T. T.; Pham, V. T.; Nguyen-Tran, T. Synthesis of Tantalum-Doped Tin Oxide Thin Films by Magnetron Sputtering for Photovoltaic Applications. *J. Electron. Mater.* **2017**, *46*, 3667−3673.

(19) Xu, Z.; Teo, S. H.; Gao, L.; Guo, Z.; Kamata, Y.; Hayase, S.; Ma, T. La-doped SnO_2 as ETL for Efficient Planar-structure Hybrid Perovskite Solar cells. *Org. Electron.* **2019**, *73*, 62−68.

(20) Park, M.; Kim, J. Y.; Son, H. J.; Lee, C. H.; Jang, S. S.; Ko, M. J. Low-temperature Solution-processed Li-doped SnO_2 as an Effective Electron Transporting Layer for High-performance Flexible and Wearable Perovskite Solar Cells. *Nano Energy* **2016**, *26*, 208−215.

(21) Bahadur, J.; Ghahremani, A. H.; Martin, B.; Druffel, T.; Sunkara, M. K.; Pal, K. Solution Processed Mo Doped SnO_2 as an Effective ETL in the Fabrication of Low Temperature Planer Perovskite Solar Cell under Ambient Conditions. *Org. Electron.* **2019**, *67*, 159−167.

(22) Yang, G.; Lei, H.; Tao, H.; Zheng, X.; Ma, J.; Liu, Q.; Ke, W.; Chen, Z.; Xiong, L.; Qin, P.; Chen, Z.; Qin, M.; Lu, X.; Yan, Y.; Fang, G. Reducing Hysteresis and Enhancing Performance of Perovskite Solar Cells Using Low-Temperature Processed Y-Doped SnO_2 Nanosheets as Electron Selective Layers. *Small* **2017**, *13*, 1601769.

(23) Ye, H.; Liu, Z.; Liu, X.; Sun, B.; Tan, X.; Tu, Y.; Shi, T.; Tang, Z.; Liao, G. 17.78% Efficient Low-temperature Carbon-based Planar

Perovskite Solar Cells Using Zn-doped SnO_2 Electron Transport Layer. *Appl. Surf. Sci.* **2019**, *478*, 417−425.
(24) Gong, X.; Sun, Q.; Liu, S.; Liao, P.; Shen, Y.; Grätzel, C.; Zakeeruddin, S. M.; Grätzel, M.; Wang, M. Highly Efficient Perovskite Solar Cells with Gradient Bilayer Electron Transport Materials. *Nano Lett.* **2018**, *18*, 3969−3977.
(25) Ren, X.; Yang, D.; Yang, Z.; Feng, J.; Zhu, X.; Niu, J.; Liu, Y.; Zhao, W.; Liu, S. F. Solution-Processed Nb:SnO_2 Electron Transport Layer for Efficient Planar Perovskite Solar Cells. *ACS Appl. Mater. Interfaces* **2017**, *9*, 2421−2429.
(26) Chen, H.; Liu, D.; Wang, Y.; Wang, C.; Zhang, T.; Zhang, P.; Sarvari, H.; Chen, Z.; Li, S. Enhanced Performance of Planar Perovskite Solar Cells Using Low-Temperature Solution-Processed Al-Doped SnO_2 as Electron Transport Layers. *Nanoscale Res. Lett.* **2017**, *12*, 238.
(27) Roose, B.; Johansen, C. M.; Dupraz, K.; Jaouen, T.; Aebi, P.; Steiner, U.; Abate, A. A Ga-doped SnO_2 mesoporous Contact for UV Stable Highly Efficient Perovskite Solar Cells. *J. Mater. Chem. A* **2018**, *6*, 1850−1857.
(28) Yang, D.; Yang, R.; Wang, K.; Wu, C.; Zhu, X.; Feng, J.; Ren, X.; Fang, G.; Priya, S.; Liu, S. High Efficiency Planar-type Perovskite Solar Cells with Negligible Hysteresis Using EDTA-complexed SnO_2. *Nat. Commun.* **2018**, *9*, 3239.
(29) Hui, W.; Yang, Y.; Xu, Q.; Gu, H.; Feng, S.; Su, Z.; Zhang, M.; Wang, J.; Li, X.; Fang, J.; Xia, F.; Xia, Y.; Chen, Y.; Gao, X.; Huang, W. Red-Carbon-Quantum-Dot-Doped SnO_2 Composite with Enhanced Electron Mobility for Efficient and Stable Perovskite Solar Cells. *Adv. Mater.* **2019**, 1906374.
(30) Liu, Z.; Deng, K.; Hu, J.; Li, L. Coagulated SnO_2 Colloids for High-Performance Planar Perovskite Solar Cells with Negligible Hysteresis and Improved Stability. *Angew. Chem.* **2019**, *58*, 11497−11504.
(31) Han, G. S.; Chung, H. S.; Kim, D. H.; Kim, B. J.; Lee, J.-W.; Park, N.-G.; Cho, I. S.; Lee, J.-K.; Lee, S.; Jung, H. S. Epitaxial 1D Electron Transport Layers for High-Performance Perovskite Solar Cells. *Nanoscale* **2015**, *7*, 15284−15290.
(32) Chen, J.; Park, N. G. Causes and Solutions of Recombination in Perovskite Solar Cells. *Adv. Mater.* **2019**, *31*, 1803019.
(33) Xie, J.; Huang, K.; Yu, X.; Yang, Z.; Xiao, K.; Qiang, Y.; Zhu, X.; Xu, L.; Wang, P.; Cui, C.; Yang, D. Enhanced Electronic Properties of SnO_2 via Electron Transfer from Graphene Quantum Dots for Efficient Perovskite Solar Cells. *ACS Nano* **2017**, *11*, 9176−9182.
(34) Tu, B.; Shao, Y.; Chen, W.; Wu, Y.; Li, X.; He, Y.; Li, J.; Liu, F.; Zhang, Z.; Lin, Y.; Lan, X.; Xu, L.; Shi, X.; Ng, A. M. C.; Li, H.; Chung, L. W.; Djurišić, A. B.; He, Z. Novel Molecular Doping Mechanism for n-Doping of SnO_2 via Triphenylphosphine Oxide and Its Effect on Perovskite Solar Cells. *Adv. Mater.* **2019**, *31*, 1805944.
(35) Zhu, Z.; Bai, Y.; Liu, X.; Chueh, C.-C.; Yang, S.; Jen, A. K.-Y. Enhanced Efficiency and Stability of Inverted Perovskite Solar Cells Using Highly Crystalline SnO_2Nanocrystals as the Robust Electron-Transporting Layer. *Adv. Mater.* **2016**, *28*, 6478−6484.
(36) Hou, M.; Zhang, H.; Wang, Z.; Xia, Y.; Chen, Y.; Huang, W. Enhancing Efficiency and Stability of Perovskite Solar Cells via a Self-Assembled Dopamine Interfacial Layer. *ACS Appl. Mater. Interfaces* **2018**, *10*, 30607−30613.
(37) Wu, W.-Q.; Chen, D.; Cheng, Y.-B.; Caruso, R. A. Thin Films of Tin Oxide Nanosheets Used as the Electron Transporting Layer for Improved Performance and Ambient Stability of Perovskite Photovoltaics. *Sol. RRL* **2017**, *1*, 1700117.
(38) Choi, K.; Lee, J.; Kim, H. I.; Park, C. W.; Kim, G. W.; Choi, H.; Park, S.; Park, S. A.; Park, T. Thermally Stable, Planar Hybrid Perovskite Solar Cells with High Efficiency. *Energy Environ. Sci.* **2018**, *11*, 3238−3247.
(39) Hu, W.; Zhou, W.; Lei, X.; Zhou, P.; Zhang, M.; Chen, T.; Zeng, H.; Zhu, J.; Dai, S.; Yang, S.; Yang, S. Low-Temperature In Situ Amino Functionalization of TiO_2 Nanoparticles Sharpens Electron Management Achieving over 21% Efficient Planar Perovskite Solar Cells. *Adv. Mater.* **2019**, *31*, 1806095.
(40) Chen, J.; Zhao, X.; Kim, S. G.; Park, N. G. Multifunctional Chemical Linker Imidazoleacetic Acid Hydrochloride for 21% Efficient and Stable Planar Perovskite Solar Cells. *Adv. Mater.* **2019**, *31*, 1902902.
(41) Zhang, Y.; Liu, X.; Li, P.; Duan, Y.; Hu, X.; Li, F.; Song, Y. Dopamine-crosslinked TiO_2/perovskite Layer for Efficient and Photostable Perovskite Solar Cells under Full Spectral Continuous Illumination. *Nano Energy* **2019**, *56*, 733−740.
(42) Gerrits, N.; Kroes, G. J. Curious Mechanism of the Dissociative Chemisorption of Ammonia on Ru (0001). *J. Phys. Chem. C* **2019**, *123*, 28291−28300.
(43) Wang, F.; Li, T.; Jiao, H. Nitridation of the Metallic Mo_2C (001) Surface from NH_3 Dissociative Adsorption-A DFT Study. *Surf. Sci.* **2019**, *689*, 121466.
(44) Xiao-Hong, L.; Shan-Shan, L.; Yong-Liang, Y.; Rui-Zhou, Z. Adsorption of NH_3 onto Vacancy-defected Ti_2CO_2 Monolayer by First-principles Calculations. *Appl. Surf. Sci.* **2020**, *504*, 144325.
(45) Kuang, A.; Ran, Y.; Peng, B.; Kuang, M.; Wang, G.; Yuan, H.; Tian, C.; Chen, H. Adsorption and Decomposition of Metal Decorated Phosphorene Toward H_2S, HCN and NH_3 Molecules. *Appl. Surf. Sci.* **2019**, *473*, 242−250.
(46) Asahi, R.; Morikawa, T.; Ohwaki, T.; Aoki, K.; Taga, Y. Visible-light Photocatalysis in Nitrogen-doped Titanium Oxides. *Science* **2001**, *293*, 269−271.
(47) Zheng, Y.; Jiang, B.; Gao, Z.; Lin, G.; Sang, N.; Chen, L.; Li, M. Optimization of SnO_2-based Electron-selective Contacts for Si/PEDOT:PSS Heterojunction Solar Cells. *Sol. Energy* **2019**, *193*, 502−506.
(48) Yang, D.; Zhou, X.; Yang, R.; Yang, Z.; Yu, W.; Wang, X.; Li, C.; Liu, S. (. F.).; Chang, R. P. H. Surface Optimization to Eliminate Hysteresis for Record Efficiency Planar Perovskite Solar Cells. *Energy Environ. Sci.* **2016**, *9*, 3071−3078.
(49) Li, X.; Dar, M. I.; Yi, C.; Luo, J.; Tschumi, M.; Zakeeruddin, S. M.; Nazeeruddin, M. K.; Han, H.; Grätzel, M. Improved Performance and Stability of Perovskite Solar cells by Crystal Crosslinking with Alkylphosphonic Acid ω-ammonium Chlorides. *Nat. Chem.* **2015**, *7*, 703−711.
(50) Si, H.; Liao, Q.; Kang, Z.; Ou, Y.; Meng, J.; Liu, Y.; Zhang, Z.; Zhang, Y. Deciphering the NH_4PbI_3Intermediate Phase for Simultaneous Improvement on Nucleation and Crystal Growth of Perovskite. *Adv. Funct. Mater.* **2017**, *27*, 1701804.
(51) Li, D.; Sun, C.; Li, H.; Shi, H.; Shai, X.; Sun, Q.; Han, J.; Shen, Y.; Yip, H. L.; Huang, F.; Wang, M. Amino-functionalized Conjugated Polymer Electron Transport Layers Enhance the UV-photostability of Planar Heterojunction Perovskite Solar Cells. *Chem. Sci.* **2017**, *8*, 4587−4594.
(52) Tian, J.; Xue, Q.; Tang, X.; Chen, Y.; Li, N.; Hu, Z.; Shi, T.; Wang, X.; Huang, F.; Brabec, C. J.; Yip, H. L.; Cao, Y. Dual Interfacial Design for Efficient $CsPbI_2$ Br Perovskite Solar Cells with Improved Photostability. *Adv. Mater.* **2019**, *31*, 1901152.
(53) Laban, W. A.; Etgar, L. Depleted Hole Conductor-free Lead Halide Iodide Heterojunction Solar Cells. *Energy Environ. Sci.* **2013**, *6*, 3249−3253.
(54) Edri, E.; Kirmayer, S.; Henning, A.; Mukhopadhyay, S.; Gartsman, K.; Rosenwaks, Y.; Hodes, G.; Cahen, D. Why Lead Methylammonium Tri-iodide Perovskite-based Solar Cells Require a Mesoporous Electron Transporting Scaffold (but Not Necessarily a Hole Conductor). *Nano Lett.* **2014**, *14*, 1000−1004.

https://dx.doi.org/10.1021/acsaem.0c00563
ACS Appl. Energy Mater. 2020, 3, 5039−5049